

ISSN: 0095-8972 (Print) 1029-0389 (Online) Journal homepage: <http://www.tandfonline.com/loi/gcoo20>


Humidity-sensing and DNA-binding ability of bis(4-benzylpiperazine-1-carbodithioato- k^2 S,S')nickel(II)

Muneeb-Ur Rehman, Muhammad Imran, Zia-Ur-Rehman, Abbas Hassan, Amin Badshah, Afzal Shah, Muhammad Nawaz Tahir & Ghani Shah

To cite this article: Muneeb-Ur Rehman, Muhammad Imran, Zia-Ur-Rehman, Abbas Hassan, Amin Badshah, Afzal Shah, Muhammad Nawaz Tahir & Ghani Shah (2015) Humidity-sensing and DNA-binding ability of bis(4-benzylpiperazine-1-carbodithioato- k^2 S,S')nickel(II), Journal of Coordination Chemistry, 68:2, 295-307, DOI: [10.1080/00958972.2014.977880](https://doi.org/10.1080/00958972.2014.977880)

To link to this article: <http://dx.doi.org/10.1080/00958972.2014.977880>

 View supplementary material 

 Accepted author version posted online: 16 Oct 2014.
Published online: 20 Nov 2014.

 Submit your article to this journal 

 Article views: 97

 View related articles 

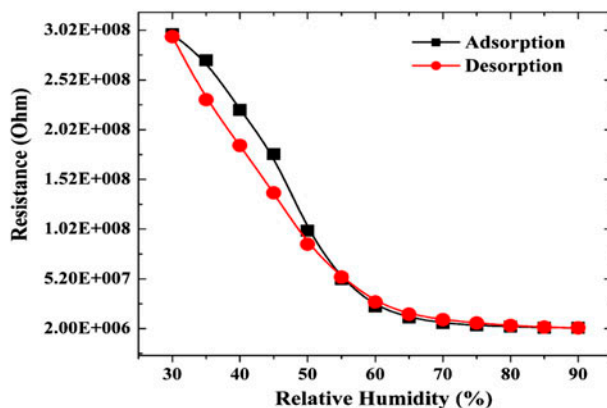
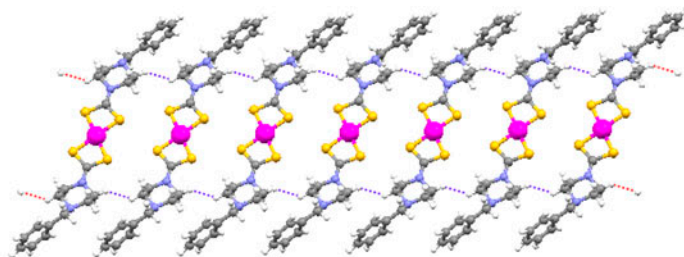
 View Crossmark data 

Humidity-sensing and DNA-binding ability of bis(4-benzylpiperazine-1-carbodithioato- k^2 S,S')nickel(II)

MUNEEB-UR REHMAN[†], MUHAMMAD IMRAN[‡], ZIA-UR-REHMAN^{*‡},
ABBAS HASSAN[‡], AMIN BADSHAH[‡], AFZAL SHAH[‡], MUHAMMAD NAWAZ
TAHIR[§] and GHANI SHAH[†]

[†]Department of Physics, Islamia College, Peshawar, Pakistan
[‡]Department of Chemistry, Quaid-i-Azam University, Islamabad, Pakistan
[§]Department of Physics, University of Sargodha, Sargodha, Pakistan

(Received 13 August 2014; accepted 2 October 2014)



The complex bis(4-benzylpiperazine-1-carbodithioato)nickel(II) was synthesized and characterized. The complex has good humidity sensing and DNA binding ability.

*Corresponding author. Email: zrehman@qau.edu.pk

Bis(4-benzylpiperazine-1-carbodithioato- k^2 S,S')nickel(II), **1**, was prepared by metathesis of sodium salt of 4-benzylpiperazine-1-carbodithioate with nickel(II) chloride in 2:1 ratio. Complex **1** was characterized by analytical techniques including elemental analysis, FT-IR, UV-visible spectroscopy, and X-ray single-crystal analysis. The latter technique confirmed square-planar geometry around Ni with the formation of NiS₄ core with two shorter and two longer Ni-S bonds. The packing diagram revealed a supramolecular chain structure mediated by unconventional H...H dihydrogen bonds that resulted in a chair and a ladder-like structure when viewed along the *a*-axis and *c*-axis, respectively. The thin-film coating resulted in a microporous film with a band gap of 1.69 eV. Complex **1**-based sensor was fabricated to check the humidity-sensing properties of the material. Resistance of the device decreased by two orders of magnitude and capacitance was enhanced with the increase of relative humidity. The DNA binding study proved **1** to be a good DNA binder with binding constant value of $1.4 \times 10^4 \text{ M}^{-1}$.

Keywords: Nickel(II) dithiocarbamate; Unconventional dihydrogen bond; Microporous thin film; Humidity sensor; DNA binding

1. Introduction

Humidity sensors have broad spectrum applications including industrial, agricultural, environmental monitoring, personal safety, national security, and automotive and aerospace industries [1]. The environmental protection awareness has led to the development of sensing technology. Humidity sensors play a pivotal role to monitor humidity in many industries, machines, and fields such as libraries, museums, clothes driers, electronic devices, air coolers, broiler forming, food and cereal stocking, and in medicine [2–4]. The resistive and capacitive humidity sensors have attracted much attention due to their high sensitivity to humidity, low cost, and excellent performance. These types of sensors can be operated over a wide range of relative humidity (RH) and temperatures. Different kinds of materials including polymers and transition metal oxides have been used for fabrication of humidity sensors [5]. An excellent humidity sensor should have broad range of operation, quick response and recovery time, low hysteresis loss, and more importantly low cost.

Cisplatin and its derivatives are well-known anticancer agents; however, serious side effects including toxicity toward normal cells and tolerance by the tumor cells have limited their usage. Side effects can be minimized or nullified by appropriate selection of ligand and metal. Dithiocarbamates moderate the cytotoxicity of platinum-based drugs through selective removal of the metal from enzyme–thiol complex by nucleophilic attack of sulfur on the platinum center. In addition to this, they have the potency to protect the normal tissues without undermining the cytostatic activity of parent drugs [5]. Similarly, nickel is more body compatible than platinum. This motivated us to synthesize a new nickel(II) dithiocarbamate and study its supramolecular association, resistive- and capacitive-type sensing properties and DNA-binding ability.

2. Experimental

2.1. Materials and methods

Nickel(II) chloride and 4-benzylpiperazine were purchased from Sigma-Aldrich Chemical Company, while CS₂ was obtained from Reidel-de-haën; all were used as received. Methanol was obtained from Fluka and dried by standard procedures [6].

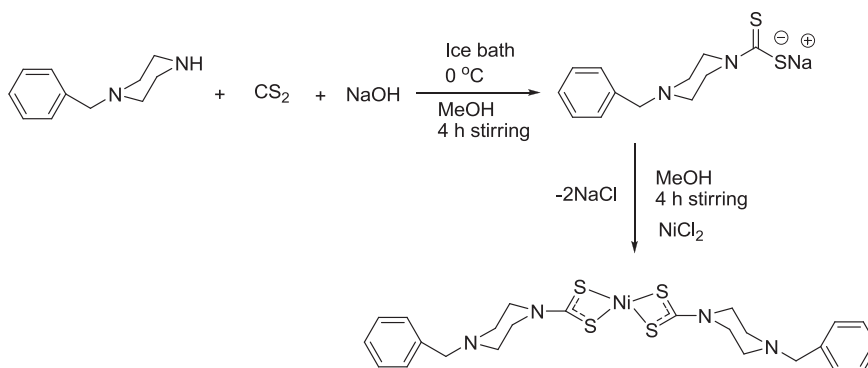
The microanalyses were performed by a Leco CHNS 932 apparatus. The melting point of the complex was taken in a capillary tube by a MP-D mitamura Riken Kogyo (Japan). The IR spectrum was determined by Thermo Nicolet-6700 FT-IR spectrophotometer from 4000 to 200 cm^{-1} . The absorption measurements were determined by a Shimadzu 1800 UV-visible spectrophotometer.

The X-ray single-crystal analysis was carried out with a Bruker Kapa APEX-II CCD diffractometer having a CCD detector set 40 mm from the crystal. From a sealed ceramic diffraction tube (SIEMENS) having graphite-monochromated Mo-K α radiation, different intensities were determined. Then using Patterson and DIRDIF method, the structure of the compound was solved. Further refinement on F^2 was carried out by full matrix least squares using SHELXL-97. For thin-film deposition, **1** was dissolved in acetone to prepare 2% solution and was then deposited on glass substrate using drop-casting technique.

2.2. Synthesis

2.2.1. Synthesis of sodium 4-benzylpiperazine-1-carbodithioate. To the solution of 4-benzylpiperazine (20 mM in methanol), equimolar amount of sodium hydroxide was added and stirred for one hour followed by dropwise addition of 1.4 mL (slight excess) CS_2 in methanol. The reaction mixture was stirred for 4 h at 0 °C and the off-white precipitates thus obtained were filtered and washed with diethyl ether as shown in scheme 1. Yield: 4.8 g, 87%, m.p. 132–133 °C, Anal. Calcd for $\text{C}_{12}\text{H}_{15}\text{N}_2\text{S}_2\text{Na}$: C, 52.52; H, 5.47; N, 10.21; S, 23.35. Found: C, 52.46; H, 5.36; N, 10.01; S, 23.27%. FT-IR (cm^{-1}): 1016 $\nu(\text{C-S})$, 1451 $\nu(\text{C-N})$.

2.2.2. Synthesis of bis(4-benzylpiperazine-1-carbodithioato- k^2 S,S')nickel(II) complex. Bis(4-benzylpiperazine-1-carbodithioato)nickel(II) was prepared according to the reported procedure [7]. The ligand was treated with nickel(II) chloride in 1 : 2 ratio using methanol as a solvent. The reaction mixture was stirred for 4 h at room temperature. The precipitates were filtered off, washed with cold distilled water, and dried under an IR lamp (scheme 1). The product was recrystallized from chloroform and dichloromethane to yield greenish crystals. Yield: 2.5 g, 82%, m.p.; 147–149 °C, Anal. Calcd for $\text{C}_{24}\text{H}_{30}\text{N}_4\text{S}_4\text{Ni}$: C, 51.34; H, 5.39; N, 9.98; S, 22.84. Found: C, 51.29; H, 5.37; N, 9.96; S, 22.83%. FT-IR (cm^{-1}) 385, $\nu(\text{Ni-S})$, 1434 $\nu(\text{C-N})$.

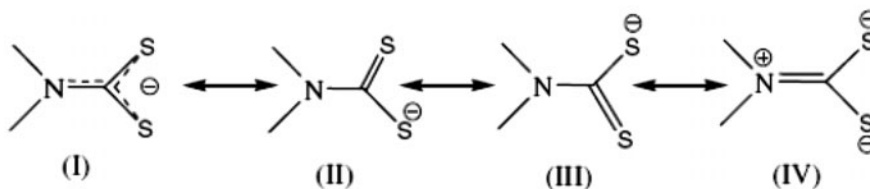


Scheme 1. Synthesis of ligand salt and bis(dithiocarbamato)nickel(II) complex.

3. Results and discussion

3.1. FT-IR spectral data

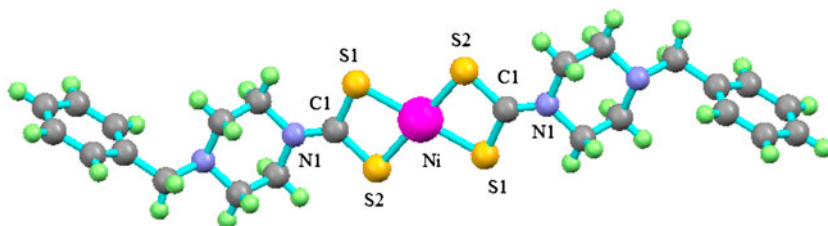
FT-IR provides valuable information about the presence of different functional groups in the compounds. Absorption at 385 cm^{-1} in the spectra of **1** can be attributed to Ni–S stretch and thus indicated complex formation. The other two important vibrations are “thioureide” band due to the N–CSS moiety and a C–S stretch. The band due to C–N stretch was observed at 1488 cm^{-1} that lies between the range reported for C–N single bond ($1250\text{--}1360\text{ cm}^{-1}$) and C=N double bond ($1640\text{--}1690\text{ cm}^{-1}$) and is an indication of partial double-bond character in the C–N bond [8, 9]. The presence of a band in the above-mentioned region for N–CSS group is due to the four possible resonance structures (scheme 2). The appearance of a single peak at 992 cm^{-1} indicated the bidentate coordination of dithiocarbamate [10, 11]. These observations are consistent with the X-ray single-crystal analysis (tables 1 and 2).



Scheme 2. Canonical forms of NCS_2 .

Table 1. Structure data and structure refinement parameter for **1**.

Crystal data	1
Chemical formula	$\text{C}_{24}\text{H}_{30}\text{N}_4\text{NiS}_4$
Crystal size (mm^3)	$0.35 \times 0.18 \times 0.16$
Formula weight (g M^{-1})	561.47
Crystal system	Monoclinic
Space group	$P2_1/c$
$T(\text{K})$	296(2)
Wavelength (\AA)	0.71073
Cell parameters	
$a(\text{\AA})$	6.5548(4)
$b(\text{\AA})$	6.5702(3)
$c(\text{\AA})$	31.4296(18)
$\alpha(^{\circ})$	90
$\beta(^{\circ})$	95.545(3)
$\gamma(^{\circ})$	90
$V(\text{\AA}^3)$	1347.22(13)
Z	2
Absorption coefficient (mm^{-1})	1.050
$F(0\ 0\ 0)$	588.0
Data collection	
2θ Range for data collection	5.2–52
Number of collected reflections	10,507
Number of independent reflections	2648
Goodness-of-fit on F^2	1.005
Final R indexes [$I \geq 2\sigma(I)$]	$R_1 = 0.0481$, $wR_2 = 0.1034$
Final R indexes [all data]	$R_1 = 0.0973$, $wR_2 = 0.1224$

Figure 1. Ball and stick diagram of **1**.Table 2. Selected bond lengths (Å) and angles (°) of **1**.

Bond lengths		Bond angles	
Ni1–S2	2.1962(11)	S2–Ni1–S2	180.00(1)
Ni1–S2	2.1962(11)	S2–Ni1–S1	79.63(4)
Ni1–S1	2.1996(11)	S2–Ni1–S1	100.37(4)
Ni1–S1	2.1996(11)	S2–Ni1–S1	100.37(4)
S1–C1	1.716(4)	S2–Ni1–S1	79.63(4)
S2–C1	1.718(4)	S1–Ni1–S1	180.00(1)
N1–C1	1.296(5)		

3.2. Crystal structure of **1**

In **1**, the nickel lies on the 2_1 screw axis with a distorted square-planar environment of the NiS_4 chromophore. The structure (figure 1) is perfectly square planar with S2–Ni–S2 and S1–Ni–S1 angles of 180° as shown in table 2. The Ni–S distances are slightly asymmetric and lie in the expected range for four-coordinate dithiocarbamates.

In **1**, the dithiocarbamate ligands are bidentate, giving four-membered chelate rings $[\text{NiS}_2\text{C}]$. The short thioureide C–N distance [$\text{C1–N1} = 1.299(5)$ Å] indicates the contribution of the double-bond character to a formally single N–C bond in the dithiocarbamate group, i.e. admixture sp^2 -hybridized state to sp^3 orbitals of the nitrogen; this would lead to a δ^+ surplus charge on the nitrogen with corresponding δ^- charge delocalized through the four-membered CS_2 M ring [12]. According to early reports, the C–N bond in dithiocarbamates is approximately equal to 1.35 Å [13]. Compound **1** shows slightly shorter C–N bonds (1.299(5) Å) confirming the complexation. These facts can be explained by the increased importance of the canonical form (IV) upon complexation (scheme 2). The C–S distances [(1.715(4) and 1.718(4) Å)] are significantly shorter than the typical C–S single-bond distance (1.81 Å) due to partial π -delocalization in the NCS_2 groups [14]. Moreover, the shorter Ni–S bond is associated with a longer C–S bond and vice versa in **1**; this is in accord with the bonding asymmetry of the ligands. The bond distances and angles are in agreement with previously reported structure for nickel(II) dithiocarbamates [15].

In the packing diagram (figure 2), intermolecular dihydrogen bond is observed with a $\text{C5–H5B}\cdots\text{H3B–C3}$ at a distance of 2.263 Å, which is shorter than the sum of the van der Waals radii for two hydrogens (2.4 Å). The presence of this interaction solely between H5B and H3B may be due to their partial positive and negative nature, respectively. As clear from figure 2, H3B is near to the electron-releasing benzyl group resulting in high electron density and H5B which is in close proximity to electron withdrawing CS_2 moiety due to its ligation to nickel, thus forming hydrogen donor acceptor pair. These two unconventional dihydrogen bonds connect the neighboring molecules to generate a supramolecular array with a Ni to Ni bond distance of 6.570 Å. In this array, the benzyl groups on either side of

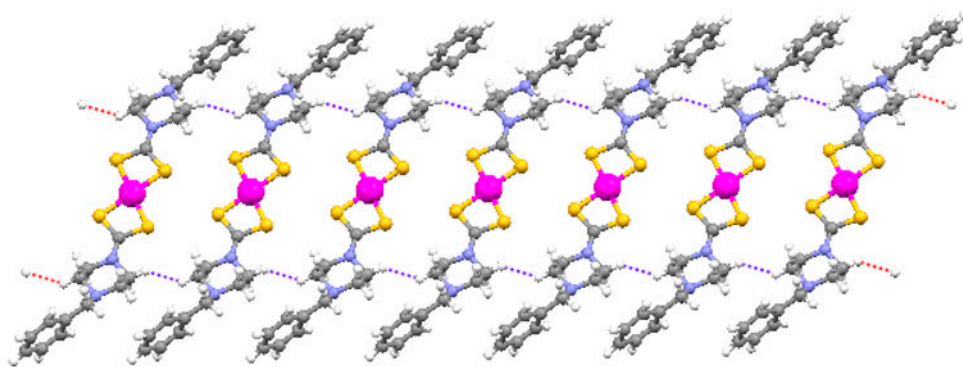


Figure 2. Supramolecular chain structure mediated by unconventional H-H bonds (2.263 Å) with a Ni-Ni bond distance of 6.570 Å.

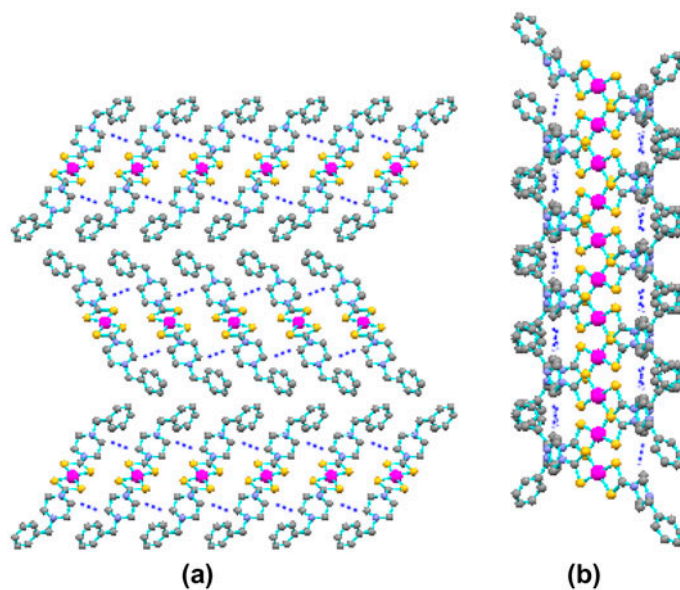


Figure 3. (a) Extension of molecules in the unit cell with a chair-like structure along the *a*-axis, (b) ladder-like structure along the *c*-axis. Hydrogens are omitted for clarity.

Ni ions are oriented in opposite direction to give a wavy nature to the chain. Extension of molecules in the unit cell give a chair shape when viewed along the *a*-axis as depicted in figure 3(a). This chain can be recognized as a ladder-like structure along the *c*-axis with NiS₄ core to make ladder steps [figure 3(b)].

3.3. The electronic spectral analysis

The electronic spectrum of **1** showed absorption bands at 13,624 cm⁻¹ (ν_1), 15,974 cm⁻¹ (ν_2), and 21,551 cm⁻¹ (ν_3) attributed to three d-d transitions $^1A_{2g} - ^1A_{1g}$, $^1B_{1g} - ^1A_{1g}$, and $^1E_g - ^1A_{1g}$, respectively, in order of their increasing energies which are expected for d⁸ system having low spin square-planar geometry (table S1, see online supplemental material at

<http://dx.doi.org/10.1080/00958972.2014.977880>). The transition around 20,000–21,000 cm^{-1} is the characteristic peak of d^8 square-planar complexes [16]. The transition at 30,581 cm^{-1} is due to intraligand $\pi-\pi^*$ transition in the complexes which occurs at 33,003 cm^{-1} in free ligand. The shift toward lower wave number is due to delocalization of charge density on dithiocarbamate after symmetrical binding of both S atoms to the metal center. Another transition at 25,445–25,510 cm^{-1} is due to charge transfer from sulfur to nickel [17].

Complex **1** shows $\pi-\pi^*$ transition at 30,581 cm^{-1} (figure S1) and ϵ value calculated from the slope (a) of the above graph is 76,000 $\text{L M}^{-1} \text{cm}^{-1}$, while the transition at 25,510 cm^{-1} is due to charge transfer phenomenon from sulfur to nickel and the ϵ value calculated from the slope (b) of the above graph is 14,000 $\text{L M}^{-1} \text{cm}^{-1}$.

3.4. Microporous film

The SEM micrographs of the as-deposited **1** are shown in figure 4(a) and (b) showing that the glass substrate is well covered by the complex. Moreover, it was observed that 2-D nanoplates are formed by the agglomeration of small particles during the deposition process of the thin film. These nanoplates are of irregular shape and sizes forming a porous structure with well-defined pore channels. The nanoplates have sizes of 2–5 μm . The large specific surface of the nanomaterials is of particular importance to the catalytic properties of the materials. The pores and pore channels play a pivotal role in the sensor applications. Zhang *et al.* [18] also observed such nanostructured plates and porous structure for NiS_{1+x} nanocrystals and noted excess sulfur in the film, which would enhance the density of active sites on the catalyst surface for hydrogenolysis [18, 19]. EDX analysis showed the presence of the following (by weight %): carbon (51.03), oxygen (10.99), sulfur (27.13), and Ni (10.84). The presence of oxygen indicates that the channels have enough volume to accommodate water. This microporous material is appropriate for humidity sensing and may find application in separation, purification, transport, gas storage, and catalysis [20].

Figure 5 shows the $F(R)^2$ versus $E(\text{eV})$ plot for **1**. The value of the band gap is obtained, using the Kubelka–Munk function [21], by extrapolating the linear part of the graph to the axis of the abscissa. This gives the band gap of 1.69 eV. Nickel sulfide and cadmium sulfide are considered promising candidates in the conversion of solar energy into electrical energy.

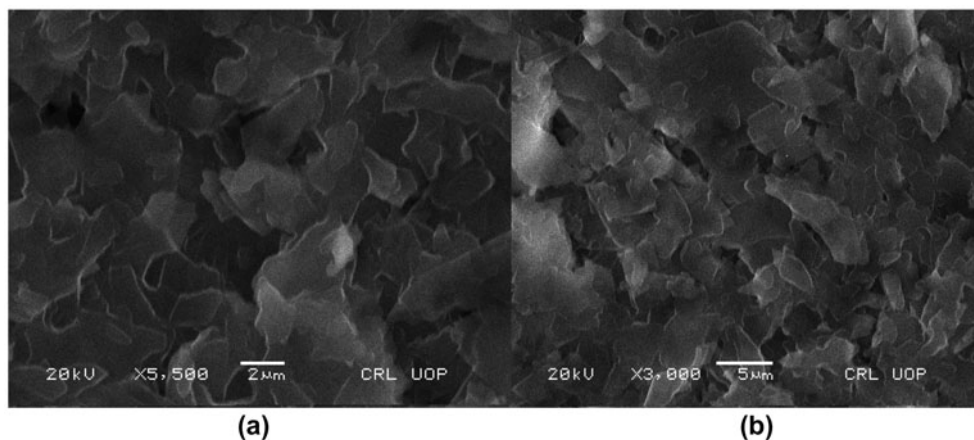


Figure 4 (a and b). SEM images of **1** thin film with different magnifications.

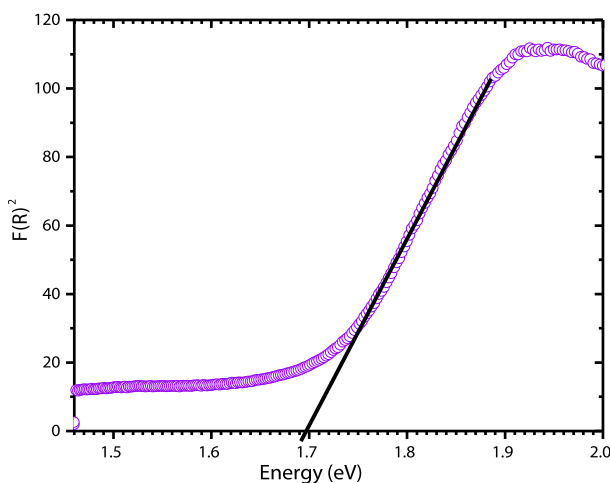


Figure 5. The optical energy gap (E_g) for **1**.

However, the band gap of CdS (2.4 eV) and NiS (0.8 eV) does not lie close to the solar energy spectrum, and thus one needs to have composite material to satisfy optical properties such as band gap matching with the solar spectrum. One of the critical contributions of this article is to provide a new approach to tune the band gap instead of taking the composite materials. The band gap of the caged nickel sulfide in **1** is shown in figure 5; the band gap is of direct nature being equal to 1.69 eV. This value lies between the band gap value of CdS (2.4 eV) and NiS (0.8 eV). Similar result of 1.65 eV was also observed taking the $(\text{NiS})_{0.75}(\text{CdS})_{0.25}$ composite film [22]. However, the present approach is unique for tuning the band gap for solar energy conversion. In the next phase of this work, this character of the band gap will be studied for solar energy conversion.

3.5. Humidity-sensing properties and sensing mechanism

A capacitive- and resistive-type humidity sensor was fabricated. The Al electrodes were deposited on the glass substrate separated with 20- μm gap. Complex **1** was deposited between the Al electrodes via drop-casting technique. The hysteresis phenomenon for sensor was tested and recorded for both resistive- and capacitive-type sensing applications at 1-kHz frequency. Resistance of the sensor decreased with increase of RH as shown in figure 6. When RH was increased from 30 to 90%, the resistance decreased by two orders of magnitude. It was found that capacitance of device increased with RH as shown in figure 7. At 90% RH, the capacitance of 0.14 nF of **1**-based sensor is comparable to 1 nF capacitance of humidity sensors made from alumina nanowire films [23] and porous silicon layer with mesa structure [24].

Due to the petal-like plate surface and porous nature of **1**, as shown in SEM image in figure 4(a) and (b), humidity was adsorbed on the surface of the material and also percolated into the pore channels present in the structure. This petal-like surface and porous nature of the **1** thin film promoted the adsorption of water. The resistance of the material was decreased due to an increase of charge carriers, electron, and hydronium H^+ , in **1** and water system. This adsorption was a two-step process, chemisorption, and physisorption, and overall process is based on ionic conduction model as illustrated in figure 8(a) and (b). The adsorbed water vapors were ionized due to back donation from d-orbitals of Ni to δ^*

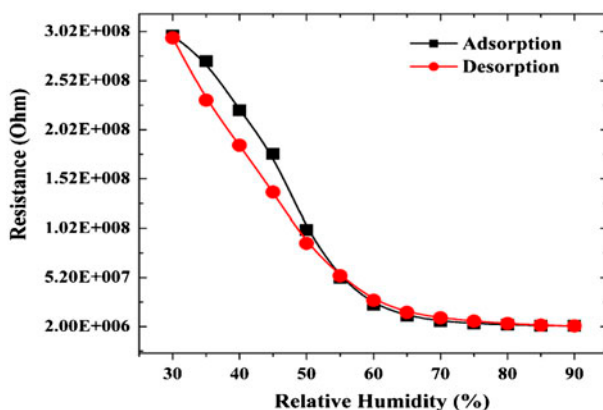


Figure 6. Resistance hysteresis characteristic of humidity sensor, based on Ni-complex material, under testing frequency of 1 kHz.

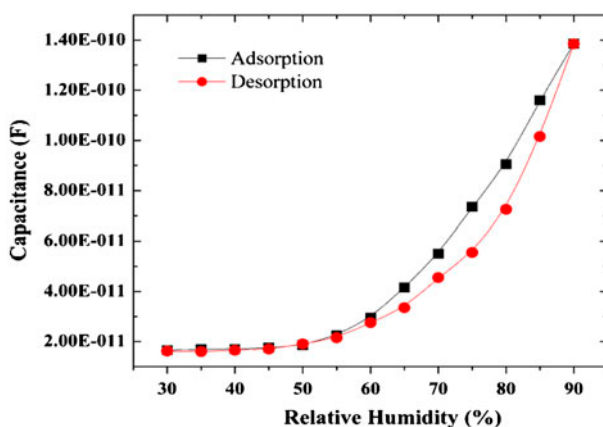


Figure 7. Capacitance hysteresis characteristic of humidity sensor, based on Ni-complex material, under testing frequency of 1 kHz.

anti-bonding molecular orbital of water molecule resulting in H^+ and OH^- . The water molecule was chemisorbed on the active sites of the **1** thin film. This first layer is overridden by the second layer of water molecules in physisorption manner in such a way that the negative dipole of the second layer is interacting with positive dipole of the first one. This hydrogen bonding prevents the water molecules of the first physisorption layer to move freely. However, these hydrogen bonds progressively diminish in the next layer making it behave like the bulk liquid water finally. In the process, the water molecules get ionized into the hydronium ion (H_3O^+) resulting in an enhancement of ionic conduction. This conduction is due to the Von Grothuss conduction mechanism [25] and is shown in figure 8(a). When RH was increased from 30 to 90%, water molecular layers added up and thus formed many liquid-like layers. These liquid-like layers facilitated the hydronium ion to dissociate into H^+ and H_2O . The H^+ ion is considered to be the dominant carrier in the high RH environment. Protons tunnel from one water molecule to another one via hydrogen

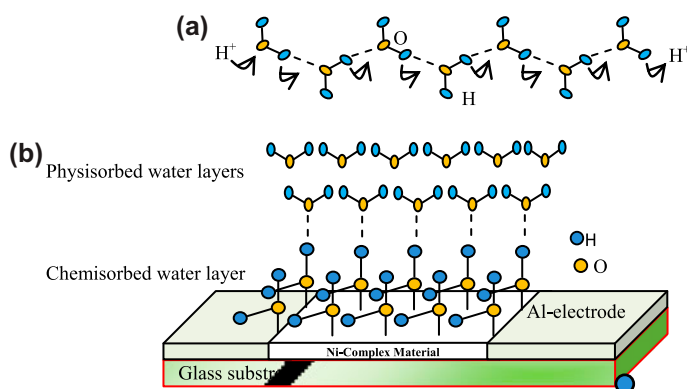


Figure 8. (a) Von Grothuss mechanism for proton conductivity, (b) chemisorption and physisorption of water-layers on the surface of **1**.

bonding that universally exists in liquid-like water layers. With the increase of RH, more layers condensed and ordering of the water molecules may gradually disappear in order to facilitate protonic conduction. At low humidity, the sensor was not sensitive because the water vapors could rarely form continuous mobile layers on the surface of the **1**-based sensor. These two immobile layers, the chemisorbed and first physisorbed ones, cannot contribute to protonic conductivity. However, they could provide electron tunneling between donor water sites. The energy induced by the surface anions facilitates the electrons to hop along the surface covered by immobile layers; the chemisorbed and first physisorbed layers contribute to overall conduction process at low humidity levels at which no effective protonic conduction contributes. The imposed electric field on the sensor also contributes to phonon-assisted hopping of the electrons from one water molecule to another at low RH [23]. Nevertheless, in the high RH environment the sensor is relatively sensitive due to the presence of H^+ ions and continuous mobile layers.

The capacitance of the device was increased because of an increase in polarity of water upon interaction with **1** thin film. This enhancement stems from bonding of water with Ni thus making the former more electron deficient, as consequence the partial positive and negative charges on hydrogen and oxygen become more intense. The polarity enhancement of the next layer can be attributed to the strengthening of hydrogen bonding between first and second layer. This layer by layer addition of water molecules contribute to the overall enhancement of the capacitance of the sensor.

3.6. DNA interaction studies

CTDNA was dissolved in 100 mL of doubly ionized water (pH 7) and stirred overnight. This solution was kept at 277 K for less than four days. The nucleotide-to-protein ratio (N/P) was obtained by taking the absorbance at 260 and 280 nm. $A_{260}/A_{280} = 1.90$ showed that DNA is appreciably free of protein. The concentration of DNA was determined from the absorbance at 260 nm using molar absorption coefficient of $6600 \text{ M}^{-1} \text{ cm}^{-1}$ and was found to be $2.3 \times 10^{-4} \text{ M}$ [26].

UV-visible titration was performed by keeping the concentration of the compound constant and varying the concentration of DNA (10, 20, 30, 40, and 50 μM). The resulting

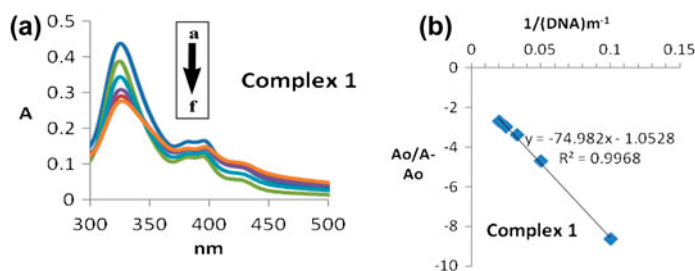


Figure 9. (a) UV-visible spectrum of **1** in the presence of DNA. (b) Plot of $A_0/(A - A_0)$ vs. $1/[DNA]$ for the determination of **1**-DNA binding constant.

DNA-compound mixture was kept at room temperature for 30 min before taking the spectrum. The cuvettes used in this experiment were of 1-cm path length.

The absorption spectra of **1** in the absence and presence of different concentrations of DNA are shown in figure 9(a). According to the literature, hyperchromism in the presence of DNA is an indication of breakage of the secondary structure of DNA and hypsochromism is due to the complex-DNA adduct formation either through electrostatic effect or intercalation [27]. By comparison of the absorbance of the compound with and without DNA [figure 9(a)], a shift was observed which provides evidence of complex-DNA interaction. The spectrum shows significant hypochromic shift in the absorption maxima of **1** by the addition of DNA. This type of shift suggests intercalation and groove mode of binding which are because of the presence of phenyl groups in the ligand that facilitate such binding.

Based upon the variation in absorbance, the binding constant of the complex with DNA was calculated using the Benesi-Hildebrand equation [28]:

$$\frac{A_0}{A - A_0} = \frac{\varepsilon_G}{\varepsilon_{H-G} - \varepsilon_G} + \frac{\varepsilon_G}{\varepsilon_{H-G} - \varepsilon_G} \times \frac{1}{K[DNA]} \quad (3.1)$$

Here, K is the binding constant, A_0 and A are the absorbances of the complex and complex-DNA adduct, respectively, and ε_G and ε_{H-G} are the absorption coefficients of the complex and the complex-DNA adduct, respectively.

The binding constant, $1.4 \times 10^4 \text{ M}^{-1}$, was obtained from the intercept-to-slope ratios of $A_0/(A - A_0)$ versus $1/[DNA]$ plots [figure 9(b)]. The binding constant is comparable to those of some intercalative Ru(II) and Ni(II) complexes [29, 30]. This may be due to the unconventional hydrogen bond [H...H (packing diagram) or $\pi \cdots \pi$ or H... π bonds] formation capability of **1**. In addition, coordinatively unsaturated Ni(II) has vacant sites available for interacting with nitrogen of the DNA bases.

4. Conclusion

This article presents a supramolecular chain structure of bis(dithiocarbamato- $k^2 S, S'$)nickel (II) complex mediated by unconventional dihydrogen bonds (2.263 Å). The supramolecular chain can be visualized as a ladder-like structure along the c -axis with Ni to Ni distance of

6.570 Å. Thin film with well-defined pore channels was developed on a glass surface with water molecules entrapped in the cavities. Such microporous materials are expected to find applications in separation, storage, transport, and catalysis. Moreover, the band gap value of 1.65 eV for microporous film may be useful for solar energy conversion. Complex **1**-based sensor was fabricated to check the humidity-sensing properties of the material. Resistance of the device decreased by two orders of magnitude and capacitance was enhanced with increase of RH. The observed capacitance of 0.14 nF is in close proximity of the reported capacitance of 1 nF of humidity sensors based on alumina nanowire films and porous silicon layer with mesa structure under testing frequency of 1 kHz. The enhancement in the capacitance is attributed to the adsorption of water molecules on the surface of the petal-like structure and pore channels observed in the SEM image. The petal-like structure provides remarkable surface area and efficient active sites for adsorption of water molecules. The protonic conductivity, for **1** and water, has been discussed on the basis of Von Grotthuss conduction mechanism. The complex has a good DNA-binding ability with binding constant of $1.4 \times 10^4 \text{ M}^{-1}$.

Supplementary material

Single-crystal X-ray diffraction data for the structural analysis have been deposited with the Cambridge Crystallographic Data Center, CCDC No. 909547. The copy of this information may be obtained free of charge from the Director, CCDC, 12 Union Road, Cambridge, CBZ 1EZ, UK (Fax: +44 1223 336033; E-mail: deposit@ccdc.cam.ac.uk or www: <http://www.ccdc.cam.ac.uk>).

Acknowledgement

We acknowledge the financial support from Higher Education Commission of Pakistan.

References

- [1] Q. Qi, T. Zhang, S. Wang, X. Zheng. *Sens. Actuators B*, **137**, 649 (2009).
- [2] E. Traversa. *Sens. Actuators B*, **23**, 135 (1995).
- [3] Z. Zhao, M. Knight, S. Kumar, E.T. Eisenbraun, M.A. Carpenter. *Sens. Actuators B*, **129**, 726 (2008).
- [4] F.H. Ramirez, S. Barth, A. Tarancon, O. Casals, E. Pellicer, J. Rodriguez, A.R. Rodriguez, J.R. Morante. *Nanotechnology*, **18**, 244016 (2007).
- [5] D.L. Bodenner, P.C. Dedon, P.C. Keng, R. Borch. *Cancer Res.*, **46**, 2745 (1986).
- [6] W.F.L. Armarego, C. Chai. *Purification of Laboratory Chemicals*, 5th Edn, Butterworth, Oxford (2003).
- [7] H. Cesur, T.K. Yazicilar, B. Bati, V.T. Yilmaz. *Synth. React. Inorg. Met.-Org. Chem.*, **31**, 1271 (2001).
- [8] S. Srinivasan, K. Ramalingam, C. Rizzoli. *Polyhedron*, **33**, 60 (2012).
- [9] S.C. Bajja, A. Mishra. *J. Coord. Chem.*, **64**, 2727 (2011).
- [10] K. Nakamoto. *Infra-red and Raman Spectra of Inorganic and Coordination Compounds*, John Wiley and Sons, New York, NY (1997).
- [11] Zia-ur-Rehman, N. Muhammad, A. Shah, S. Ali, A. Meetsma. *J. Coord. Chem.*, **65**, 3238 (2012).
- [12] A.V. Ivanov, T. Rodyna, O.N. Antzutkin. *Polyhedron*, **17**, 3101 (1998).
- [13] R.S. Amim, M.R.L. Oliveira, G.J. Perpétuo, J. Janczak, L.D.L. Miranda, M.M.M. Rubinger. *Polyhedron*, **27**, 1891 (2008).
- [14] L. Ronconi, L. Giovagnini, C. Marzano, F. Bettio, R. Graziani, G. Pilloni, D. Fregona. *Inorg. Chem.*, **44**, 1867 (2005).

- [15] K. Ramalingam, K. Radha, G. Aravamudan, C. Mahadevan, C. Subramanyam, M. Seshasayee. *Acta Cryst. C*, **40**, 1838 (1984).
- [16] A.B.P. Lever *Inorganic Electronic Spectroscopy*, p. 333, Elsevier, Amsterdam (1968).
- [17] R. Bhaskaran, K. Ramalingam, G. Bocelli, A. Cantoni, C. Rizzoli. *J. Coord. Chem.*, **61**, 1710 (2008).
- [18] H.T. Zhang, G. Wu, X.H. Chen. *Mater. Lett.*, **59**, 3728 (2005).
- [19] A. Olivas, J. Cruz-Reyes, V. Petranovskii, M. Avalos, F. Fuentes. *J. Vac. Sci. Technol.*, **A16**, 3515 (1998).
- [20] R.G. Zarracino, H.M.G. Rodríguez. *Cryst. Growth Des.*, **9**, 1651 (2009).
- [21] M. Bagheri-Mohagheghi, N. Shahtahmasebi, M.R. Alinejad, A. Youssefi, M. Shokooh-Saremi. *Physica B*, **403**, 2431 (2008).
- [22] A.U. Ubale, A.N. Bargal. *Mater. Res. Bull.*, **46**, 1000 (2011).
- [23] Z. Feng, X. Chen, J. Chen, J. Hu. *J. Phys. D: Appl. Phys.*, **45**, 225305 (2012).
- [24] S. Kim, J. Park, S. Lee, S. Yi. *J. Phys. D: Appl. Phys.*, **33**, 1781 (2000).
- [25] O.K. Arghese, D.W. Gong, M. Paulose, K.G. Ong, C.A. Grimes, E.C. Dickey. *J. Mater. Res.*, **17**, 1162 (2002).
- [26] Y. Zhang, X. Wang, L. Ding. *Nucleos. Nucleot. Nucl.*, **30**, 49 (2011).
- [27] M. Patel, M. Chhasatia, P. Parmar. *Eur. J. Med. Chem.*, **45**, 439 (2010).
- [28] Zia-Ur Rehman, A. Shah, N. Muhammad, S. Ali, R. Qureshi. *Eur. J. Med. Chem.*, **44**, 3986 (2009).
- [29] X.W. Liu, J. Li, H. Deng, K.C. Zheng, Z.W. Mao, L.N. Ji. *Inorg. Chim. Acta*, **358**, 3311 (2005).
- [30] N. Raman, K. Pothiraj, T. Baskaran. *J. Coord. Chem.*, **64**, 4286 (2011).